Fine-Scale Acoustic Tomographic Imaging of Shallow Water Sediments

Dezhang Chu, Dajun Tang, Thomas C. Austin, Alan A. Hinton, *Member, IEEE*, and Richard I. Arthur, Jr.

***Abstract*—An acoustic tomographic system capable of performing *in situ* two-dimensional (2-D) acoustic imaging of shallow water sediments is described. This system is capable of resolving inhomogeneities greater than 10 cm and differentiating sound-speed variations greater than 2%. A tomographic inversion is performed in a 2-D vertical slice of about 1 m^2 (1 m $\times$ 1 m) using three identical probes, with each consisting of 20 evenly distributed transducers. In normal deployments, two of the probes are oriented vertically and are separated by about 1 meter, and the third is positioned horizontally right above the two vertical probes. The additional horizontal probe greatly improves the horizontal resolution of the system compared to conventional crosshole tomographic setups. Numerical simulations are performed to evaluate the influences of arrival time detection error and transducer position error on the performance of the tomography system. For an arrival time of 500 ns (standard deviation) and a position error of 4 mm (standard deviation), sound-speed anomalies of greater than 0.8% can be correctly predicted near the upper portion (close to the horizontal probe) and are resolvable near the lower portion. A controlled laboratory experiment was conducted to evaluate the performance of the system. The location of a polyurethane block (Conap EN22) used as a known target is correctly predicted while the inverted sound speed is about 9% lower than that from its actual value. Field data taken from a saturated muddy site are presented and analyzed. The inverted mean sound speed and attenuation are about 1480 ms^{-1} and 20 dBm^{-1}, respectively.**

***Index Terms*—Acoustic imaging, acoustic tomography, acoustic velocity measurement, inverse problem, sediments.**

I. INTRODUCTION

ACOUSTIC properties of marine sediments are of great interest and importance to underwater acousticians and marine geophysicists. A large number of publications concerning laboratory and field measurements of marine sediments have provided substantial knowledge toward our understanding of the acoustic properties of marine sediment [1]–[6]. A major shortcoming of these measurements is that the data lack continuous coverage over spatial regions of interest. Tomography has been widely used to obtain continuous maps of many acoustical, geophysical, and oceanographical parameters [7]–[18]. Recently, this technique has been applied to sediment imaging that covers the surficial sediment layer [19], [20].

Manuscript received December 6, 1999; revised August 30, 2000. This work was supported by the Office of Naval Research under Grant N00014-95-1-0408. This is the Woods Hole Oceanographic Institution Contribution 10102.

D. Chu and T. C. Austin are with the Department of Applied Ocean Physics and Engineering, Woods Hole Oceanographic Institution, Woods Hole, MA 02543 USA.

D. Tang is with the Applied Physics Laboratory, University of Washington, Seattle, WA 98105 USA.

A. A. Hinton is with Sonetech Corporation, Bedford, NH 03110 USA.

R. I. Arthur, Jr. is at P.O. Box 78, Falmouth, MA 02540 USA.

Publisher Item Identifier S 0364-9059(01)01733-2.

In mapping sound speed and/or attenuation in sediments, crosshole tomography is probably the most commonly used technique [9], [12], [19]. Conventional crosshole tomography involves two (2-D) or more (3-D) vertical transducer arrays with a mapped region from a few meters up to hundreds of meters. The spatial resolution, which is limited by the applied acoustical frequency and the geometric dimension of the mapped region, is in general in the order of meters [11], [14], [19]. However, in many acoustic applications involving high-frequency sonar systems, the acoustic wavelength is in the order of centimeters [21]–[25]. The inhomogeneous structure of the acoustic properties in the top sediment layer ($<$1 m), such as sound speed and attenuation, could have considerable influences on both monostatic and bistatic scattering [22], [24]–[29]. To better describe the scattering by such sub-bottom inhomogeneities quantitatively, a finer scale characterization of the acoustic properties of the surficial sediments (on the order of one meter and with centimeter resolution) is required. Clearly, the scales used in conventional crosshole tomography do not provide the necessary resolution for high-frequency acoustic applications.

Furthermore, crosshole tomography uses only two vertical arrays; the horizontal resolution and the robustness of the inversion strongly depend on the ratio of the vertical scale to the horizontal scale. If this ratio is small, the resultant horizontal resolution from the crosshole tomography will be poor and may not differentiate the small-scale horizontal variabilities observed in the surficial sediments [6], [20]. Rajan *et al.* [30] conducted a crosshole tomography experiment in the Arctic in 1989 to image the sound speed in sea ice. To improve the horizontal resolution, a horizontal array whose element separation was 1 m was used in between the vertical arrays whose element separation varied from 0.25 to 1 m. A total of 22 transducers were used in an imaging region of about 13 m^2 (about 9 m^2 in the ice and 4 m^2 in the water). They achieved 0.3-m vertical resolution and 0.6-m horizontal resolution, respectively, in the upper portion of the imaging region where the ray coverage is higher. More recently, a broadband (1 Hz–15 kHz) tomography system was constructed at the University of Miami GeoAcoustic Laboratory (UMGAL) and was used in a pilot experiment off Ft. Pierce, FL, in 1995 [20]. The system consists of three linear arrays, each having 16 elements at 10-cm intervals. The resultant spatial resolution is 20 cm. However, its horizontal resolution is limited due to a lack of vertical rays, an inherent deficiency of the conventional crosshole tomography.

A sediment acoustic tomographic system which can provide a fine-scale spatial resolution of the surficial unconsolidated sediment is presented in this paper. The system consists of three probes (arrays), two vertical probes resembling the crossholes configuration, and an additional horizontal probe that provides more rays with large grazing angles. It is capable of achieving a spatial resolution up to a few centimeters and differentiating a few percent variations in sound speed within the tomographic region. To evaluate the performance of the system, extensive numerical simulations are performed. Issues related to the detection errors of arrival time and the uncertainty in transducer positions are addressed. A controlled laboratory experiment involving a known scatterer was conducted to test the performance of the imaging system. Data and inversion results from a field experiment are also presented and discussed in this paper.

The paper is organized as follows. Theoretical background is provided in Section II. The newly developed fine-scale acoustic tomography system is described in Section III. In Section IV, numerical simulations are presented to evaluate the performance of the system using realistic parameters, while the laboratory and field experimental data are analyzed in Section V. Conclusions are given in Section VI.

II. Background of Sound Speed and Attenuation Tomography

Acoustic tomography is a technique with which the images representing certain acoustic properties in a specified region can be determined indirectly. This technique is always associated with solving an inversion problem, and in most cases, a linear inversion is sufficient. Although the technique involving a more sophisticated and computationally intensive diffraction tomography, in which the entire wave field is to be determined, has been reported by many investigators [8], [13], [31]–[34], a travel-time or ray-based representation of the linear system is chosen for our current applications [35]. It is worth noting that the imaging system itself will not be affected by the choice of inversion techniques.

In acoustic tomography, several approaches have been used to solve a linear inversion problem, including the weighted damped-least-square (WD-LSQ) method [36], [37], algebraic reconstruction technique (ART) [7], [38], and the simultaneous iterative reconstruction technique (SIRT) [10], [39]. Lakshminarayanan and Lent [39] have shown that SIRT is essentially equivalent to the WD-LSQ. The ART, a technique often used in medical tomography, uses local (along individual rays) minimization, and in general, converges slower than the methods using global minimization (on all possible rays) such as WD-LSQ or SIRT. In this paper, we chose WD-LSQ to solve the linear inversion problem.

A. Sound Speed Tomography

To obtain a sound-speed image, we start with the integral equation which relates the acoustic slowness s and arrival time t

$$t = \int_\Gamma s(\mathbf{r})|d\mathbf{r}| \tag{1}$$

where $\mathbf{r}$ is the position vector and Γ stands for the particular ray path corresponding to the arrival time t. In obtaining the above equation, the applicability of the ray approximation is implied, i.e., the sound-speed variation has been assumed to be small over the scale of an acoustic wavelength [40].

To proceed from (1) and simplify the analysis, the following assumptions are used throughout the paper:

- straight ray path;
- single ray path;
- no dispersion.

The first assumption requires that the sound-speed gradient in the sediment over an aperture of 1 m be small. The second assumption requires all multiple rays are resolvable in the time domain. The last assumption allows one to ignore waveform distortion due to diffraction, multiple scattering, and strong frequency-dependent attenuation.

Applying the above assumptions to (1) and discretizing the equation, a linear relation between the slowness and the arrival time can be expressed in a matrix form as

$$\mathbf{t} = D\mathbf{s} \tag{2}$$

where $\mathbf{s} = [s_1\ s_2\ \cdots\ s_m]^T$ and $\mathbf{t} = [t_1\ t_2\ \cdots\ t_n]^T$ are vectors of the slowness and the measured arrival time, respectively. Integers n and m are the number of rays and number of inversion cells, respectively. The matrix D is the kernel with a dimension of $n \times m$, whose element D_{ij} is the distance within the jth inversion cell for the ith ray. The symbol T stands for matrix transpose.

The inversion problem of (2) is underdetermined, even-determined, or overdetermined for $n < m$, $n = m$, and $n > m$, respectively. For an underdetermined inversion problem, the solution will be nonunique. To avoid the nonuniqueness, more rays than unknowns (averaged sound speeds in the inversion cells) are needed. However, since the arrival times are not fully independent of each other, the overall problem is mixed, i.e., some of the cells are overdetermined and the rest are underdetermined. The objective function to be minimized for such a mixed problem is a combination of the weighted least-square and weighted minimum-length criteria and can be expressed as [36]

$$Q = (\mathbf{t} - D\mathbf{s})^T W_d(\mathbf{t} - D\mathbf{s}) + \lambda(\mathbf{s} - \langle\mathbf{s}\rangle)^T W_s(\mathbf{s} - \langle\mathbf{s}\rangle) \tag{3}$$

where W_d and W_s are data (arrival times) and model (slowness) weighting functions (matrices), respectively. W_d defines the relative contribution of the error associated with each individual ray to the total prediction error. $W_{d_{ij}}$ stands for the relative contribution of the arrival time error of the jth ray to the arrival time error of the ith ray. If the errors are uncorrelated, the data weighting matrix is a diagonal matrix. Similarly, $W_{s_{ij}}$ defines the relative contribution of the model estimation error of the jth cell to the model estimation error of the ith cell. Since the sound speed is almost always spatially correlated, the model weighting matrix W_s is in general not a diagonal matrix. The explicit forms of the two weighting matrices are discussed in Sections III and IV. The function $\langle\mathbf{s}\rangle$ is an *a priori* estimate of slowness and λ is a damping factor. We differentiate (3) with respect to $\mathbf{s}$ and solve for $\mathbf{s}$ by setting the differentiation to zero

$$\mathbf{s} = \langle\mathbf{s}\rangle + [\lambda W_s + D^T W_d D]^{-1} D^T W_d(\mathbf{t} - D\langle\mathbf{s}\rangle). \tag{4}$$

If we designate an *a priori* estimate of the slowness $\langle \mathbf{s} \rangle$ in the above equation as the slowness estimated from the nth iteration, an iterative WD-LSQ linear inversion solution for a mixed problem can be written as

$$\mathbf{s}^{(n+1)} = \mathbf{s}^{(n)} + \left[\lambda^{(n)} W_s + D^T W_d D\right]^{-1} D^T W_d \left(\mathbf{t} - D\mathbf{s}^{(n)}\right) \tag{5}$$

where the damping factor λ is a function of iteration number. The variance matrix is found to be

$$\mathbf{C}_{ss} = \langle (\mathbf{s} - \langle \mathbf{s} \rangle)^T (\mathbf{s} - \langle \mathbf{s} \rangle) \rangle = G^{-g} G^{-gT} \tag{6}$$

where G^{-g} is the generalized inverse [36]

$$G^{-g} = [\lambda W_s + D^T W_d D]^{-1} D^T W_d. \tag{7}$$

In many situations, the precise positions of the transducers can deviate from their designed positions as a result of structural deformation during deployment (e.g., when the vertical probes are pressed into sediment). Such unavoidable errors in transducer positions will affect the accuracy of sound-speed inversions. To compensate for this type of error, (5) needs to be modified. To establish the explicit relation between the slowness and the relative position changes, we first assume that the transducers have a small amount of deviation from their original positions. These deviations are treated as unknowns in the inversion process [9], [11], [30]. We then differentiate the governing equation, (2), and replace small increments $d\mathbf{t}$, $d\mathbf{s}$, and $d\mathbf{p}$ with $\Delta\mathbf{t}$, $\Delta\mathbf{s}$ and $\Delta\mathbf{p}$, respectively

$$\begin{aligned} \Delta\mathbf{t} &= D\Delta\mathbf{s} + \frac{\partial \mathbf{t}}{\partial \mathbf{p}} \Delta\mathbf{p} \\ &= \left[D \ \frac{\partial \mathbf{t}}{\partial \mathbf{p}} \right] \begin{bmatrix} \Delta\mathbf{s} \\ \Delta\mathbf{p} \end{bmatrix} \end{aligned} \tag{8}$$

where

$$\Delta\mathbf{p} = \begin{bmatrix} \Delta\mathbf{x} \\ \Delta\mathbf{z} \end{bmatrix} \tag{9}$$

with $\mathbf{x} = [x_1 \ x_2 \ \cdots \ x_{n_p}]^T$, $\mathbf{z} = [z_1 \ z_2 \ \cdots \ z_{n_p}]^T$ being the coordinate vectors of the transducers, and n_p the number of transducers. The second term in the first square bracket of (8) is the vector form differentiation with respect to a vector and is defined as

$$\frac{\partial \mathbf{t}}{\partial \mathbf{p}} \equiv \begin{bmatrix} \frac{\partial t_1}{\partial x_1} & \frac{\partial t_1}{\partial x_2} & \cdots & \frac{\partial t_1}{\partial x_{n_p}} & \frac{\partial t_1}{\partial z_1} & \frac{\partial t_1}{\partial z_2} & \cdots & \frac{\partial t_1}{\partial z_{n_p}} \\ \frac{\partial t_2}{\partial x_1} & \frac{\partial t_2}{\partial x_2} & \cdots & \frac{\partial t_2}{\partial x_{n_p}} & \frac{\partial t_2}{\partial z_1} & \frac{\partial t_2}{\partial z_2} & \cdots & \frac{\partial t_2}{\partial z_{n_p}} \\ & & \cdots & & & \cdots & & \\ \frac{\partial t_n}{\partial x_1} & \frac{\partial t_n}{\partial x_2} & \cdots & \frac{\partial t_n}{\partial x_{n_p}} & \frac{\partial t_n}{\partial z_1} & \frac{\partial t_n}{\partial z_2} & \cdots & \frac{\partial t_n}{\partial z_{n_p}} \end{bmatrix}. \tag{10}$$

The explicit expression of $\partial t_i / \partial x_j$ and $\partial t_i / \partial z_j$ are given in the Appendix.

To simplify the matrix expression of the final solution, we define the vector $\mathbf{m}$ as a new composite model vector and the matrix K as a new composite kernel. The former includes both the slowness $\mathbf{s}$ and position coordinates vector $\mathbf{p}$ [not to be confused with the constant m which is the number of inversion cells defined in the paragraph following (1)]. The latter consists of the segment distance matrix D and the matrix of the arrival time derivative with respect to the position coordinate, $\partial\mathbf{t}/\partial\mathbf{p}$

$$\mathbf{m} = \begin{bmatrix} \Delta\mathbf{s} \\ \Delta\mathbf{p} \end{bmatrix}, \qquad K = \left[D \ \frac{\partial \mathbf{t}}{\partial \mathbf{p}} \right]. \tag{11}$$

Following the same procedures from (3)–(5), the new iterative WD-LSQ solution is found to be

$$\begin{aligned} \mathbf{m}^{(n+1)} = \ & \mathbf{m}^{(n)} + \left[\lambda^{(n)} W_m + K^{(n)^T} W_d K^{(n)}\right]^{-1} \\ & \cdot K^{(n)^T} W_d \left(\mathbf{t} - K^{(n)} \mathbf{m}^{(n)}\right) \end{aligned} \tag{12}$$

where W_m is the new model weighting function (matrix). In this case, the distance matrix D is no longer a constant matrix but rather the one that is revised for each iteration. The variance matrix, (6), is therefore a function of the iteration number. The sound-speed difference can be obtained using the following relation

$$\Delta\mathbf{c} = -\frac{\Delta\mathbf{s}}{\mathbf{s}^2}. \tag{13}$$

Since arrival time $\mathbf{t}$ is not a linear function of the position vectors $\mathbf{p}$, (8) is valid only for small position fluctuations (first order approximation). Therefore, (12) and (13) are applicable only to cases where the position errors are small, which is true for the current applications.

B. Attenuation Tomography

The amplitude of the received signal A can be expressed in terms of the amplitude of the transmitted signal as

$$A_{w,\,s} = A_0 \exp\left(-\tfrac{1}{2} \int_\Gamma \alpha_{w,\,s}(\mathbf{r}) |d\mathbf{r}|\right) \tag{14}$$

where A_0 is the amplitude measured at a reference distance, usually 1 m, in water, α is the attenuation coefficient in sediment in neper/m, and $\mathbf{r}$ is the position vector along the ray path Γ. The subscripts w and s stand for water and sediment, respectively. By ignoring the attenuation in water, we can solve (14) for α_s

$$\int_\Gamma \alpha_s(\mathbf{r}) |d\mathbf{r}| = -2 \ln\left(\frac{A_s}{A_w}\right). \tag{15}$$

By defining the ratio of the received amplitude in sediment and that in water as

$$a_{r_j} \equiv -2 \ln\left(\frac{A_s}{A_w}\right) \tag{16}$$

where ln is the natural logarithm. The matrix form solution can be obtained by discretizing (15)

$$\mathbf{a}_r = D\alpha_s \tag{17}$$

where D is the same as in (2). In contrast to the sound-speed inversion, the impact of position errors on the outcome of the attenuation inversion is less important since the amplitude of the received waveform is not sensitive to the position errors.

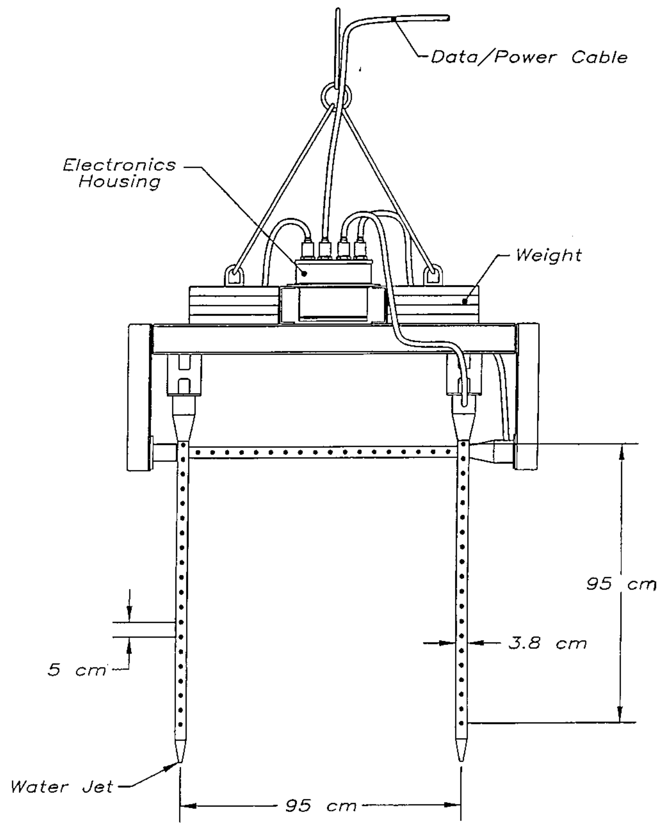

Fig. 1. Schematic diagram of the fine-scale acoustic imaging system.

Therefore, our attenuation inversion model ignores the position error and the interation scheme can be expressed explicitly as

$$\alpha_s^{(n+1)} = \alpha_s^{(n)} + \left[\lambda^{(n)} W_\alpha + D^T W_d D\right]^{-1} \cdot D^T W_d \left(\mathbf{a}_r - D^{(n)} \alpha_s^{(n)}\right) \quad (18)$$

where W_α is still the model weighting function as in (5).

III. System Descriptions

The acoustic tomographic system consists of three identical 1-m-long probes which are attached to a rigid frame and connected to a subsea electronics pressure housing (Fig. 1). The subsea electronics module contains a transmitting unit, a receiving unit, and a microcontroller for multiplexer and gain control. A multiconductor cable connects the subsea electronics pressure housing to a surface PC via an analog data line and a serial port for surface–subsea communications. A small power supply is the only other surface equipment required to operate the subsea electronics.

Each probe consists of 20 evenly spaced transducers (channels) separated by 5 cm. The transducer ceramics are free flooded cylindrical rings, with a resonance frequency around 90 kHz and an approximately 40 kHz (transmit and receive) composite bandwidth (Fig. 2). The transducers have a toroidal vertical beam pattern with their longitudinal axes perpendicular to that of the probe itself (their azimuthal beam pattern is omnidirectional), so that their beam patterns are aligned with

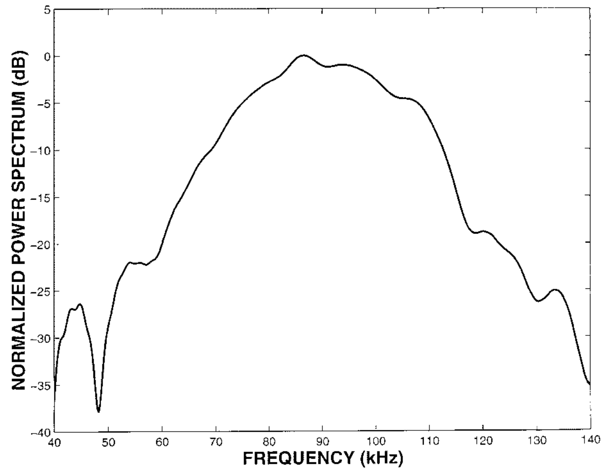

Fig. 2. Typical composite spectrum of a pair of transducers.

the imaging plane. The exact beam pattern is not important since only the relative amplitudes will be used in the inversions. The cylindrical elements are potted in polyurethane, suspended between two high-strength steel stiffening bars. The diameter of the probe is 3.81 cm, expanded slightly at the top to accommodate the interface circuitry and connector pigtail. A long and thin printed circuit board extends along the entire length of the probe, outside of one of the steel bars. In addition, a stainless steel tube connected to the probe tip is used to allow the use of a water jet for assistance in penetrating hard sediment. Table I lists several key specifications of the system.

Each transducer (channel) is capable of either transmitting or receiving, but not both at the same time. Once a channel on a probe is selected as the transmitter, transducers on the other two probes can be sequentially selected as receivers. Since there are 20 transducers on each probe, the total number of possible independent rays are 1200 (Fig. 3). The two vertically mounted probes together with the third horizontally mounted probe provide a basis for a better horizontal resolution and a more robust inversion result than that from the conventional crosshole tomography. The imaging region encompassed by the three probes is about 1 m^2. It is obvious that the upper portion of the imaging region has more ray coverage than the lower portion. It is not surprising that such an uneven ray coverage results in a higher spatial resolution in the upper imaging region as compared to the lower imaging region.

A surface PC is used to control the entire system. A Windows-based data acquisition software (Visual Basic) is used to select settings relevant to the data acquisition such as transmit and receive channels, number of pings/channel, programmable gain, and other system parameters. During data acquisition, individual transducers are selected by the data acquisition software for transmit and receive, and a specified number of pings are transmitted. The received analog data are amplified, sent to the PC, digitized with a 12-b A/D data acquisition board (National Instrument) installed on the PC, and then stored on the hard disk for post processing.

Our goal is to resolve inhomogeneities of about 5–10 cm in size and with 2% sound-speed variation. To this end, assuming

TABLE I
SPECIFICATIONS OF THE ACOUSTIC IMAGING SYSTEM

No. of probes	3 (2 vertical and 1 horizontal)
No. of transducers/probe	20
Transducer (channel) separation	5 cm
Center frequency	90-100 kHz
Transducer bandwidth (3 DB)	40 kHz (composite)
Transmit waveform	4 selectable waveforms
Source level output	170 DB re 1 μP @ 1 meter
Receiver sensitivity	-210 DB re 1 V/μP
Equivalent input noise	40 DB re 1 μP / $\sqrt{Hz}$
Beam pattern	toroidal in the vertical plane and approximately 45^o horizontally due to the printed circuit board and the steel stiffening bars
sampling rate	1 MHz
sample digits	12 bits
dynamic range	120 DB (peak signal) with 1 Hz bandwidth noise

square cells are used in the inversion, the required arrival time resolution is approximately

$$|\Delta t| \approx \left(\frac{d}{c}\right)\left(\frac{\Delta c}{c}\right)\left(\frac{d}{L}\right) \tag{19}$$

where d is the cell size, L the probe length, and c the sound speed. Inserting $\Delta c/c = 0.02$, $L = 1.0$ m, and $c = 1500$ ms^{-1}, we obtain

$$|\Delta t| \approx \begin{cases} \left(\frac{0.1}{1500}\right)(0.02)\left(\frac{0.1}{1.0}\right) \approx 133.3 \text{ (ns)}, \\ d = 0.1 \text{ m} \\ \left(\frac{0.05}{1500}\right)(0.02)\left(\frac{0.05}{1.0}\right) \approx 33.3 \text{ (ns)}, \\ d = 0.05 \text{ m} \end{cases} \tag{20}$$

for cell size of 10 and 5 cm, respectively. Since the highest sampling rate of the A/D board is 1 MHz, or 1.0 μs of sampling interval, the original raw data cannot provide the required sampling rate. To overcome this difficulty, we take advantage of the finite bandwidth of the transmit signal, which is centered at around 90–100 kHz with about 40-kHz bandwidth. For 1-MHz sampling frequency with a 20-MHz clock rate, the Nyquist frequency is 500 kHz, about four times higher than the maximum transmit frequency, and the jitter of the waveform is 50 ns. The amplitude at greater than 300 kHz is essentially flat (with randomly distributed spikes on the spectrum) and believed to be due solely to background noise. The level is about 65 dB below the maximum value (not shown in Fig. 2). Therefore interpolation using FFT/IFFT with zero padding is expected to provide satisfactory time resolution required by (20). In actual data processing, the signal used for arrival time detection has a time resolution of 10 ns (a factor of 100 interpolation).

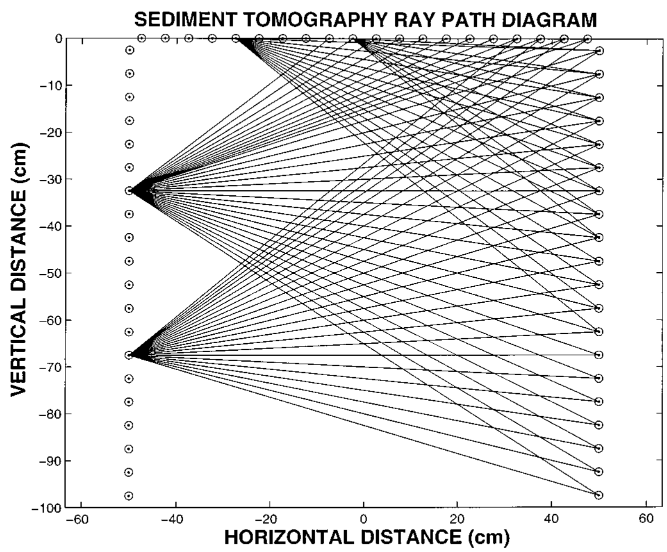

Fig. 3. Ray path diagram. Probe 1 is on the left and probe 3 is on the right. The channel (transducer) numbers are numbered from the bottom to the top. The horizontal probe is probe 2 and channels are numbered from left to the right. In the diagram, each transmit channel corresponds to several reception channels.

IV. NUMERICAL SIMULATIONS

In this section, a series of simulations are performed and the inversion results are discussed. In each simulation, a number of iterations are performed until a specified threshold (the rms model difference between ith and $(i+1)$th) is reached. All simulation parameters are chosen to be consistent with those of the actual acoustic imaging system specified in the previous section.

There are two major sources of error that affect the accuracy and robustness of our inversion results: unavoidable arrival time detection error and the uncertainty in transducer positions. To evaluate the system performance, a synthetic sound-speed model is used. This model includes seven simulated rectan-

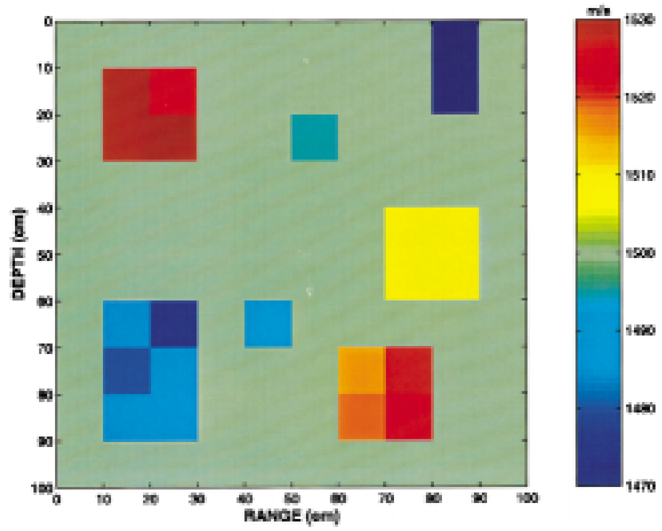

Fig. 4. Exact sound-speed image. Sound-speed anomaly is less than 2%.

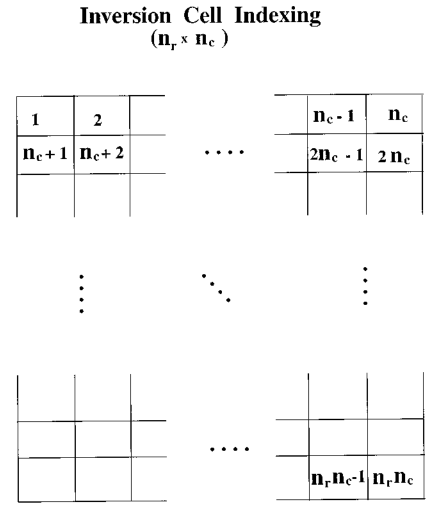

Fig. 5. Diagram of inversion cell indexing, where n_r and n_c are the numbers of cells in each column and the numbers of cells in each row, respectively.

gular regions whose sound speeds differ from the background sound speed (Fig. 4). This synthetic model is chosen to be more complicated than those used by many previous investigators [10]–[12]. The maximum sound-speed variation of the synthetic model is 2%, the tomographic area is 1.0 m $\times$ 1.0 m, and the total number of channels is 60 (20 on the top, left, and right sides of the region, respectively). The inversion cell size is chosen to be 10 cm, yielding a 10 $\times$ 10 inversion grid system. The iterative approaches given by (5) and (12) are used. The damping factor λ is allowed to decrease with the number of iterations to allow a better fit to the arrival time data [14]

$$\lambda = \alpha^n \lambda_0 \tag{21}$$

where λ_0 is the initial damping factor that controls the smoothness of the reconstructed sound speed [16], $\alpha < 1$ is the reduction constant, and n is the iteration number. As $n \rightarrow \infty$, $\lambda \rightarrow 0$. As for the data and model weighting matrices W_d and W_m, the explicit forms could be different depending on the actual problem and the assumed properties of the inhomogeneities [36], [30]. In the current application, the data weighting matrix W_d in the simulation is chosen to be an identity matrix. The model weighting matrix W_m is chosen to specify the spatial continuity condition such that the model itself or its spatial derivative is a continuous function. To perform the inversion using (5), a systematic indexing system of the inversion cells needs to be determined. There are a total of $n_c \times n_r$ grid cells used in the inversion, i.e., $n_c n_r$ unknowns, where n_c and n_r are the number of cells in each row and column, respectively. Cell index increases from the left to the right and from the top to the bottom (Fig. 5). Note that larger indices of the inversion cell correspond to the lower portion of the imaging region.

A. Errors in Arrival Time Detection

To evaluate the sensitivity of the sound-speed inversion to the errors in arrival time Δt, we assume Δt follows a Gaussian distribution with zero mean, and a standard deviation of σ_t. In the simulations, randomly generated Δt_j is added to the arrival time of the jth ray. A total of ten realizations are used for each σ_t to generate a mean inverted sound-speed image using (5). The two parameters λ_0 and α are chosen to be 1e$-$8 and 0.8, respectively. Two examples of the simulation results are shown in Fig. 6(a) and (b), where the thin solid lines are the synthetic sound-speed model and the thick solid lines are the inversion results. In Fig. 6(a), $\sigma_{\Delta t}$ is set to be zero while in Fig. 6(b), $\sigma_{\Delta t}$ is set to be 500 ns. Transducer positions are assumed to be precise and therefore errors associated with positions are not included. The agreement between the synthetic model and the inverted sound speed is excellent [Fig. 6(a)]. Only small wiggles (<0.05%) are present when cell index >85, corresponding to the lower portion of the image region (away from the horizontal probe), where the poorest inversion results are expected. Evidently, the inversion results shown in Fig. 6(b) are deteriorated compared with those in Fig. 6(a). However, the anomalous features of sound speed are still captured from the inversion. The errors become more pronounced as the cell index increases. The variations of sound-speed mismatch (standard deviation in Δc) as a function of arrival time detection error $\sigma_{\delta t}$ can be approximately characterized by a straight line from a linear regression [Fig. 6(c)]. The slope of the regression line is about 4.9 ms$^{-1}\mu$s^{-1}. Therefore, a 2% variation in sound speed (30.0 ms^{-1}) could be identified if the $\sigma_{\Delta t} < 2$ μs, assuming a detection threshold ratio of 3 : 1 is used, i.e., the inverted standard deviation in sound speed σ_c is three times larger than the potential inversion error $\sigma_{\Delta c}$. For a sampling interval of 1.0 μs (without FFT/IFFT interpolation discussed in Section III), a 2.0-μs arrival time tolerance is found to be reasonable.

B. Errors in Transducer Positions

When the probes are buried in the sediment, the precise positions of the transducers are unknown. As discussed in Section II, the position errors can be corrected using (12). Indexing of the transducers is described in Table II.

To simulate the position error, as in the arrival time simulations, a Gaussian distributed position error with zero mean is used. Again, ten realizations are used to generate an averaged inversion result. To add position errors, we further assumed that

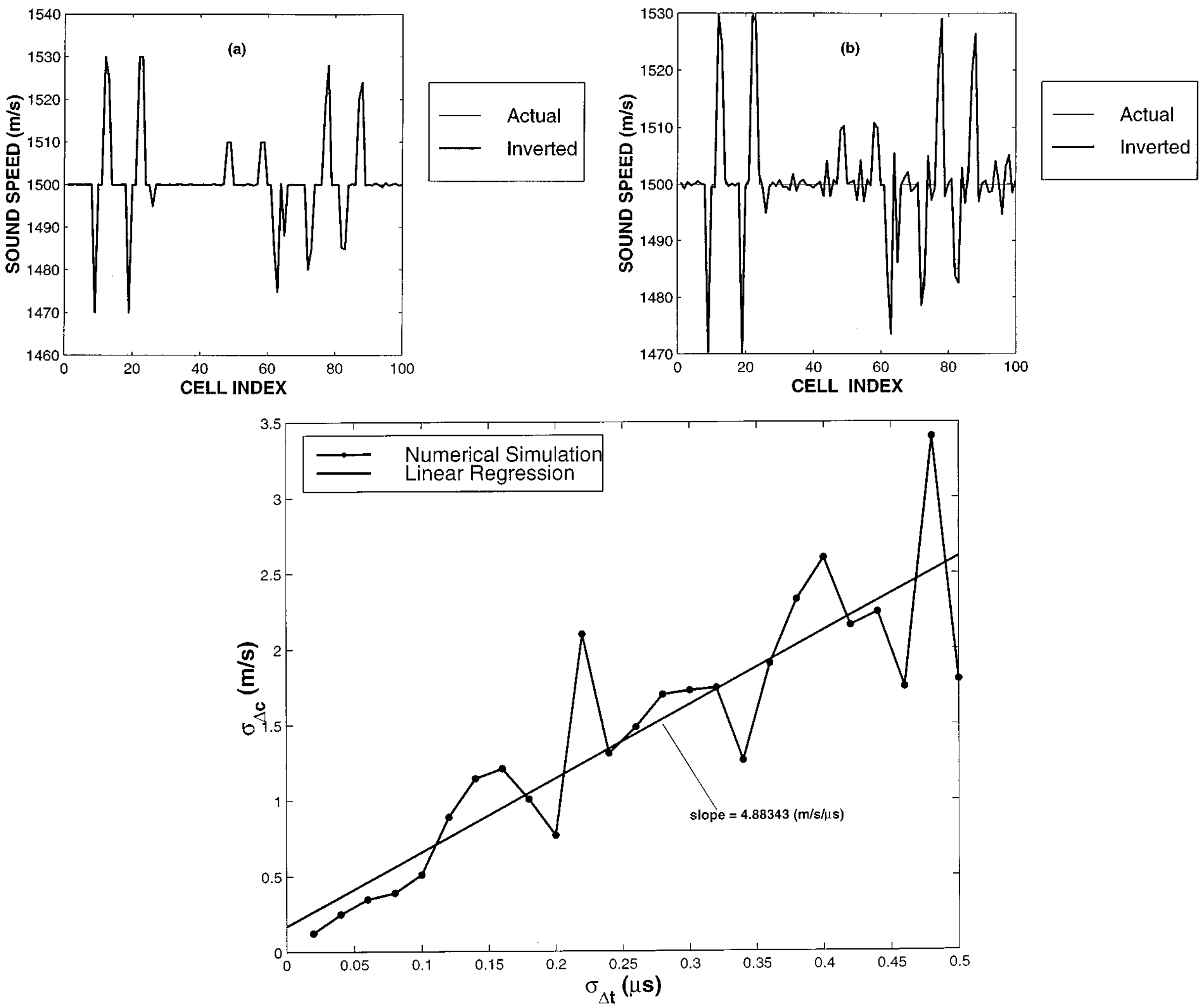

(c)

Fig. 6. Comparison of the exact sound-speed inversion using (5). The total number of the inversion grid cells is 10 $\times$ 10, with 10-cm spatial resolution. The model weighting matrix is chosen to be a flatness matrix [36], while the data weighting matrix is chosen to be an identity matrix. The initial damping factor λ_0 and the reduction factor α are chosen to be 1e$-$8 and 0.8, respectively. Uncertainties in transducer positions are set to zero. Standard deviations due to arrival time detection are set to (a) 0 ns and (b) 500 ns, respectively. Ten realizations were averaged to generate the results for each designated arrival time detection error. For each realization, only two iterations were used since more iterations provided essentially the same results, indicating a fast convergence. The thin solid line is the synthetic model while the thick solid line is from the numerical simulation. (c) Standard deviation of sound speed versus standard deviation of arrival time detection error. The dotted-solid line is from the simulation while thick solid line is the linear regression.

TABLE II
SCHEME OF TRANSDUCER INDEXING

indexes	probe/channels
1-20	probe 1: x (ch. 1 - ch. 20)
21-40	probe 2: x (ch. 1 - ch. 20)
41-60	probe 3: x (ch. 1 - ch. 20)
61-80	probe 1: z (ch. 1 - ch. 20)
81-100	probe 2: z (ch. 1 - ch. 20)
101-120	probe 3: z (ch. 1 - ch. 20)

Δx and Δz have the same probability density function (PDF), i.e., $\sigma_{\Delta x} = \sigma_{\Delta z}$. If the position correction algorithm is not used, a small amount of position error (standard deviation of 4 mm) will distort the reconstructed sound-speed image substantially and the features of the original synthetic model are almost completely lost [Fig. 7(a)]. If the position correction algorithm (12) is used, the inversion results are greatly improved [Fig. 7(b) and (c)]. The dots in Fig. 7(c) are the differences between the original positions and the true positions before inversion, i.e., position errors due to erroneous initial position estimation. The solid line is the position errors after position correction. In the simulations, the position errors in the y direction (out of the imaging plane, i.e., x–z plane) are ignored since they are of higher order error since $\Delta t \propto (\Delta y)^2$ for small Δy. Clearly, by including position correction formulation, (12), the inversion result is greatly improved and the position errors resulting from the incorrect initial position estimate have been corrected.

When the position errors are doubled to $\sigma_{\Delta x} = \sigma_{\Delta z} = 8$ mm, the inverted sound speed has larger variations compared with those in Fig. 7(b), but all seven sound speed anomalous blocks can still be clearly identified [Fig. 7(d) and (e)]. In addition, the position errors have been substantially reduced when compared with the original position errors [dots in Fig. 7(e)]. Unlike the

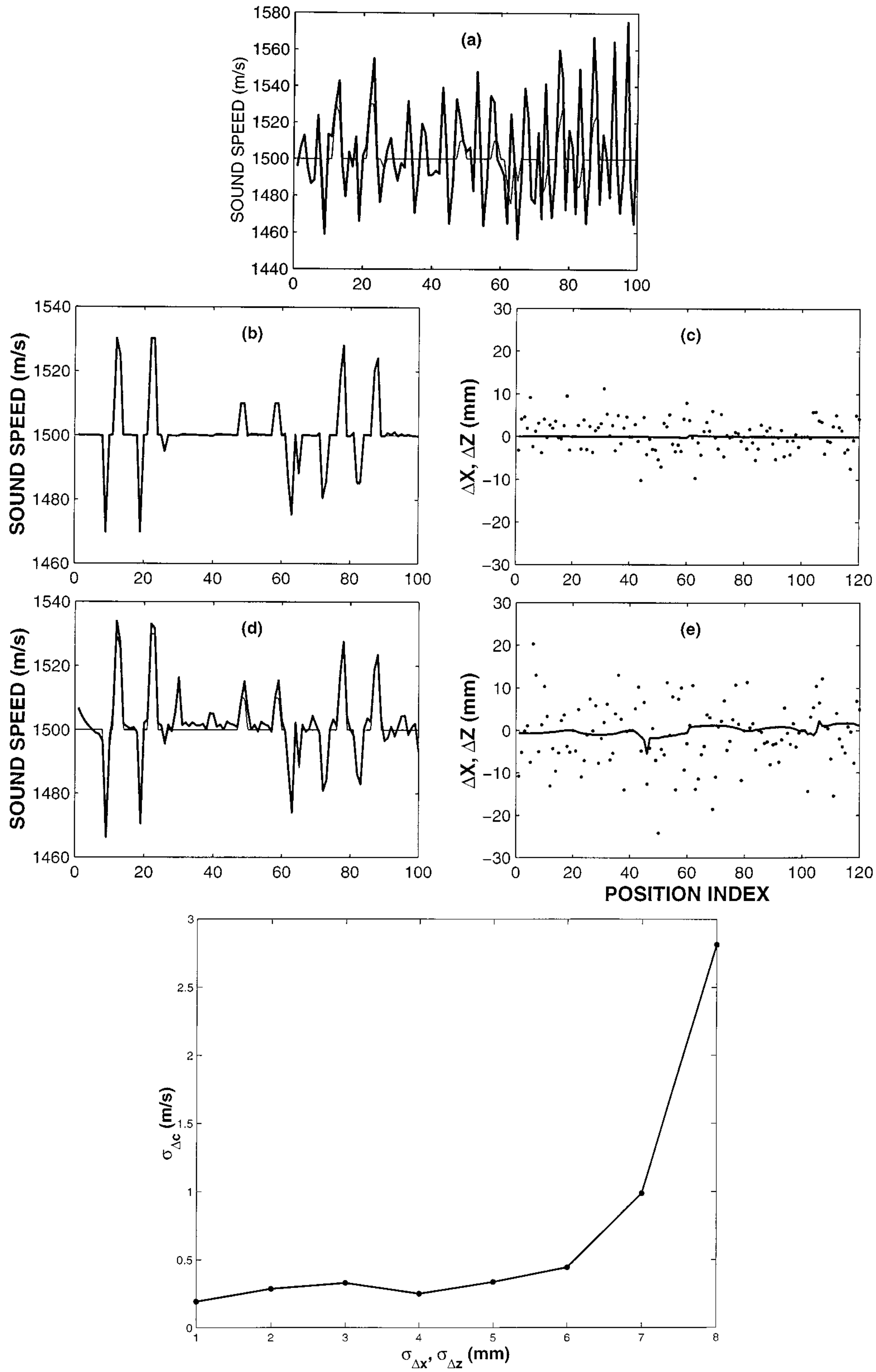

(f)

Fig. 7. Similar to Fig. 6 except that the position errors are included and the arrival time detection error is set to zero. The inversion parameters are the same as those specified in the caption of Fig. 6 except that ten iterations were needed to obtain reasonable convergence. (a) Inversion is performed using (5) (no position correction), the standard deviation of the position errors is $\sigma_{\Delta x} = \sigma_{\Delta z} = 4$ mm. (b) and (c) are the same as (a) but using (12) to incorporate the position error correction. The thin solid line is the synthetic model while the thick solid line is from the numerical simulation. (d) and (e) are the same as (b) and (c) except that $\sigma_{\Delta x} = \sigma_{\Delta z} = 8$ mm. (f) Standard deviation of the sound speed versus the standard deviation of the position error.

results for the case of zero position error [Fig. 6(c)], the relationship between $\sigma_{\Delta c}$ and the position errors $\sigma_{\Delta x}$ and $\sigma_{\Delta z}$ is nonlinear since the kernel K is a function of the transducer positions and is modified after every iteration [Fig. 7(f)].

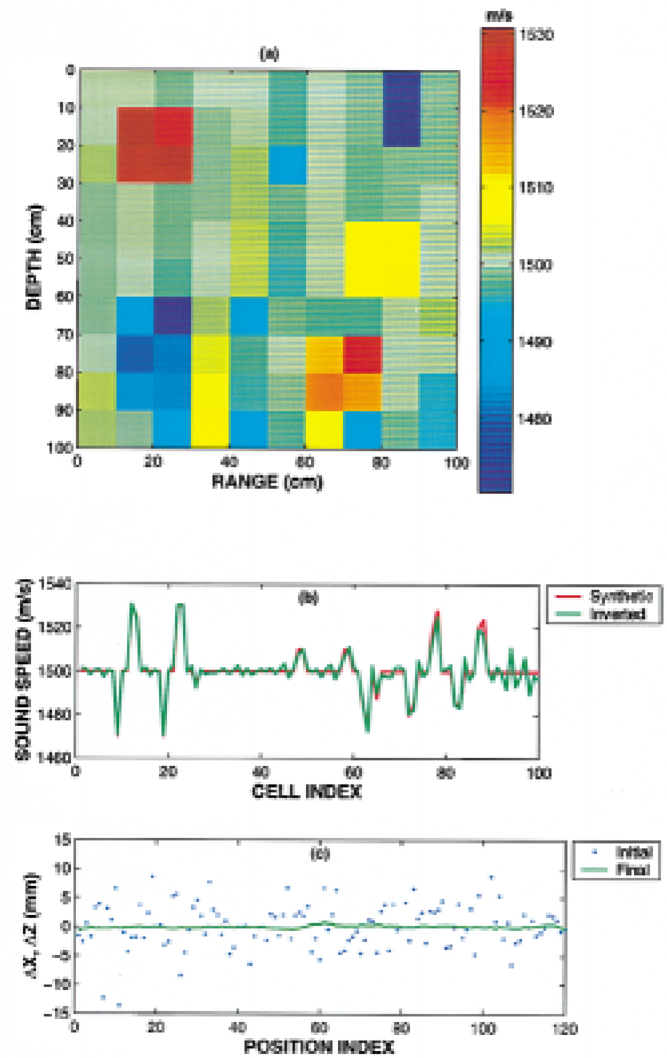

Fig. 8. Tomographic result using (12) to incorporate the position error corrections. Both the arrival time error and the position error are included. The standard deviations of arrival time error and position error are $\sigma_{\Delta t} = 0.5\ \mu$s, and $\sigma_{\Delta x} = \sigma_{\Delta z} = 4$ mm, respectively. Other inversion parameters are the same as Fig. 6. (a) Tomographic image. (b) Sound-speed versus cell indices. (c) Position errors, where the dots are initial position error while the solid line is the final (corrected) position errors.

Simulation results for a more realistic case are shown in Fig. 8, where arrival time error $\sigma_{\Delta t}$ is 500 ns and position error $\sigma_{\Delta x} = \sigma_{\Delta z}$ is 4 mm. For a system with sampling frequency of 1 MHz, and a spatial aperture of 1 m, these choices of $\sigma_{\Delta t}$, $\sigma_{\Delta x}$, and $\sigma_{\Delta z}$ can be considered reasonable. Although Fig. 8(a) looks much messier compared with Fig. 4, a careful inspection reveals that the basic structure has been captured. The agreement between the inverted and synthetic models is reasonably good, especially for cells whose indices are smaller than 80. For cell indices greater than 80, or for cells closer to the lower portion of the image region, the mismatch becomes larger and is comparable with the sound-speed anomalies that are less than 0.8%. In other words, near the lower portion of the image region, a sound-speed anomaly less than 0.8% is unlikely to be correctly predicted unless using a lower spatial resolution. Fig. 8(b) is similar to Fig. 7(b), indicating that in this case the arrival time error is the dominant source of error. The position errors have been reduced substantially [Fig. 8(c)].

V. Experiments

In this section, two data sets are analyzed, one from a laboratory experiment and the other from a field experiment.

A. Laboratory Experiment

Since the spatial scale involved in the crosshole tomography is usually several meters or larger [11], [19], [20], [30], [41], laboratory experiments with scales the same as field applications are not practical. As a result, only numerical simulations are frequently used in evaluating the performance of a particular tomography system. However, numerical modeling is still an idealized approach in which effects such as ray bending, multipath, and diffraction are ignored (see original model assumptions specified in Section II). To test the actual performance of a tomographic system, controlled laboratory experiments are desirable.

A laboratory experiment was conducted in a 2.45 m $\times$ 3.65 m $\times$ 1.50 m tank filled with sea water to about 20 cm from the top. During the tank experiment, the imaging system was horizontally placed in the tank about 65 cm (middle of the water column) from the bottom. A cylindrical polyurethane block (Conap EN22) of 14.5-cm diameter and 7.3-cm height was placed near the center. The axis of the cylinder is perpendicular to the image plane (parallel to the normal of the image plane). The measured sound speed in the water and the polyurethane block are 1507 $\pm$ 4.0 ms^{-1} (17 °C) and 1816 $\pm$ 11.0 ms^{-1}, respectively.

A 100-μs linear frequency modulated signal from 70 to 130 kHz was used for tomographic imaging of the polyurethane block. The purpose of using of a broadband chirp signal is to gain a higher signal-to-noise ratio (SNR) over the usable bandwidth. A total of 1200 arrival times were obtained from independent transmit/receive combinations via a post-processing program using Matlab. The arrival times were picked in a semiautomatic mode, or interactive mode. Because some transmit/receive transducer pairs are very close to each other, the arrival times are not resolvable due to the finite bandwidth of the transducer. These rays are therefore excluded in the tomographic inversion. The number of usable rays is 1056. A total of 30 pings are acquired for each ray and the corresponding travel time is determined from the waveform averaged over the 30 pings. It is required that the errors caused by arrival time pickup must be smaller than the arrival time anomaly due to the sound-speed anomaly of the inhomogeneity itself, i.e., 133 ns for a 10-cm inhomogeneity with 2% sound-speed anomaly [see (20)]. By applying a 100-to-1 FFT/IFFT interpolation described in Section III [paragraph following (20)], a typical ping-to-ping arrival time variation has a standard deviations of less than 50 ns, which is less than the tolerable standard deviation of arrival time error for a 2% sound-speed anomaly.

The inversion region was divided into 20 $\times$ 20 mesh grids with each being a 5 cm by 5 cm cell. The values of the diagonal data weighting matrix W_d are determined by the SNR for the corresponding acoustic ray, i.e., $W_{d_j} = \mathrm{snr}_j$, where snr_j is the SNR in linear scale for the jth ray. In other words, a ray that has higher SNR was weighted more in the inversion. Other inversion

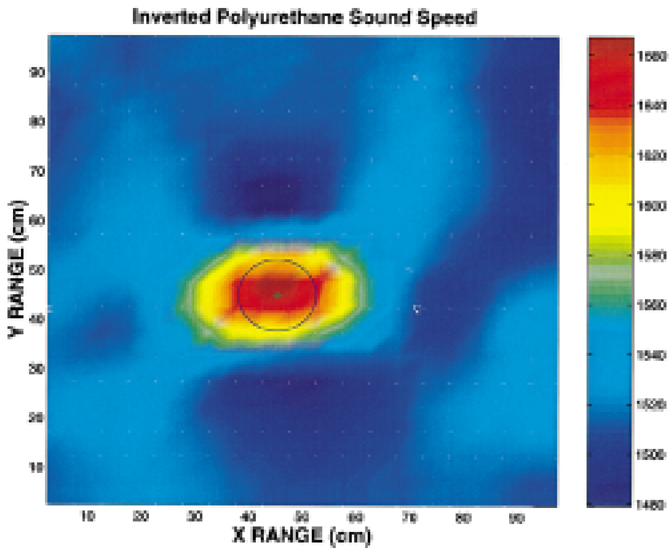

Fig. 9. Sound-speed tomographic results of polyurethane (EN22) in a water-filled tank. The size of the inversion cell is a square of 5 cm × 5 cm, 20 × 20 cells. The diagonal values of the data weighting matrix W_d are determined by the SNR for the corresponding acoustic ray, i.e., the ray that has higher SNR was weighted more in the inversion. The initial damping factor $\lambda_0 = 0.8$. The other inversion parameters are the same as those specified in the caption of Fig. 8 except that 30 iterations were used, despite that iterations more than ten did not provide significant improvement. The actual position and size of the polyurethane are marked by the solid-line circle.

parameters (α and λ_0) are the same as those used in the previous section except for the number of iterations being 30 since more cells are used in this inversion. The sound-speed image of the laboratory experiment clearly locates the polyurethane block (Fig. 9). The predicted sound speed at the center of the anomaly is 1667 ms^{-1}, or about 9% lower than the measured sound speed in the polyurethane (1816 ms^{-1}). This mismatch may be attributed to the diffraction by the polyurethane block. To obtain more accurate inversion results, the diffraction tomography should be used [13], [31], [32], [34].

B. Field Experiment

A field experiment was conducted at Hadley Harbor near Woods Hole, MA, in November 1996 on board R/V Asterias. The water depth was about 15 m, the temperature was about 20 °C, and the bottom a fluid-like soft mud. Samples of the bottom sediment were taken from the experiment site. The sediment color was black, indicating rich in decomposed organic substances. A few pieces of broken shells were found in the sample. A three-hundred-pound weight was added to the probe frame to help the probe penetrate into the sediment. Divers were used to assist and guide the probe penetration. A 200-foot-long cable was used to connect the subsea electronics unit to the surface units (PC, power supply, and data acquisition connection box).

A full set of calibration (1200 rays) in water was conducted off the dock at the Woods Hole Oceanographic Institution (WHOI) one day before the cruise. One day after the cruise, a partial calibration involving a number of selected channels were performed at the same location. One complete data set in sediment was acquired during the cruise. As in the tank experiment, a 100-μs chirp signal (70–130 kHz) was used

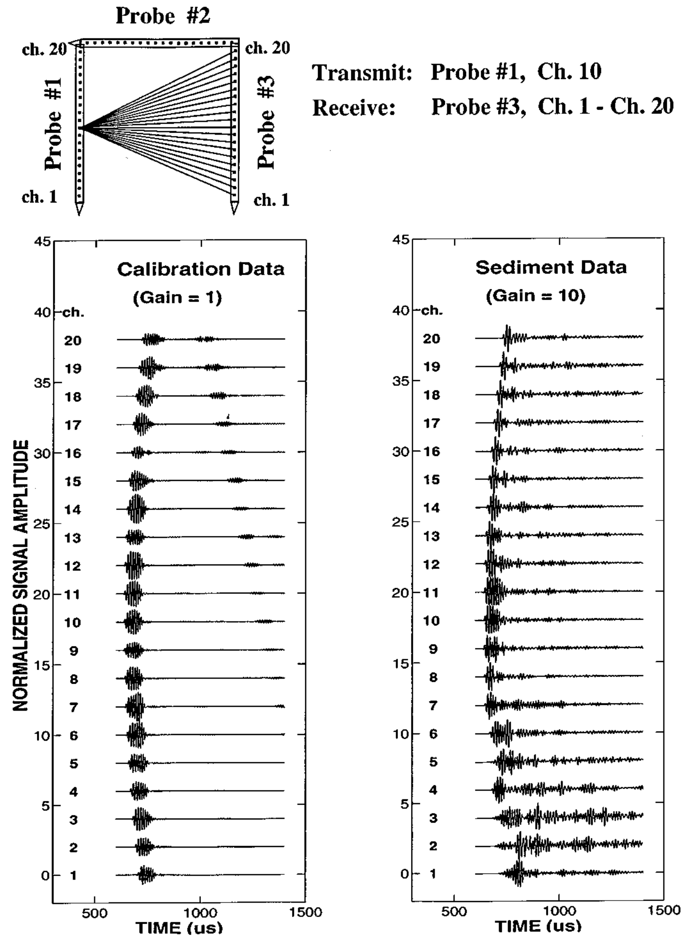

Fig. 10. Raw acoustic data time series. Left: calibration data. Right: mud data. The transmission channel is channel 10 of probe 1 while receive channels are channel 1–20 of probe 3. The programmable gain is 1 for the calibration data and 10 (20 dB) for the mud data.

as the transmit signal, and a total of 1200 transmit/receive pairs were recorded, with a 30-ping average for each pair. During data acquisition, digitized waveforms were monitored on the computer screen to ensure data quality. An example of waveforms collected in the water and sediment is shown in Fig. 10. Multiple arrivals, obvious in the water calibration data from channels 6–20, result from reflections and scattering from the metal frame, but can be easily resolved from the primary arrivals. The arrival times obtainable from the primary waveforms vary smoothly following a hyperbolic curve due to changing distance from the transducer.

In contrast, the raw time series collected in the sediments demonstrate several different characteristics. First, on every channel there are multiple arrivals which interfere with the primary waveforms, resulting in distorted waveforms. Second, the amplitudes are roughly 20 dB lower than those in the calibration mode (the gain is unity or 0 dB for calibration and is 10 or 20 dB for sediment data). Third, the arrival times do not follow a hyperbolic curve, especially in channels 1–6. Finally, some enhanced later arrivals can be observed on the channels near the bottom while the primary arrivals are greatly attenuated (channels 2 and 3). All of these indicate a heterogeneous sediment.

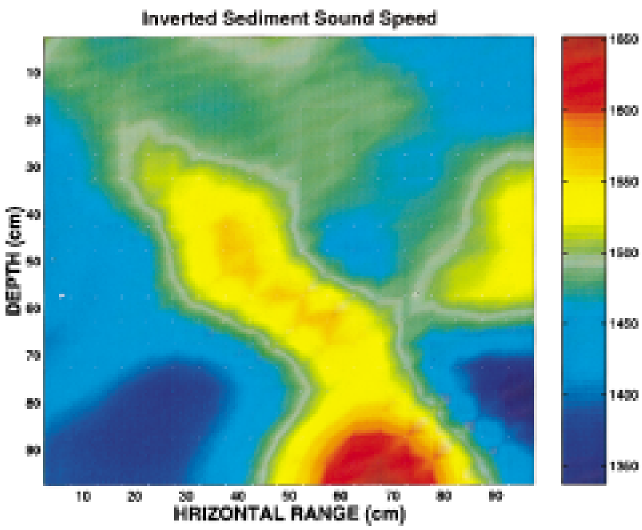

Fig. 11. Sound-speed tomographic image of muddy sediment at Hadley Harbor, MA, using (12). The inversion parameters are the same as those specified in the caption of Fig. 11.

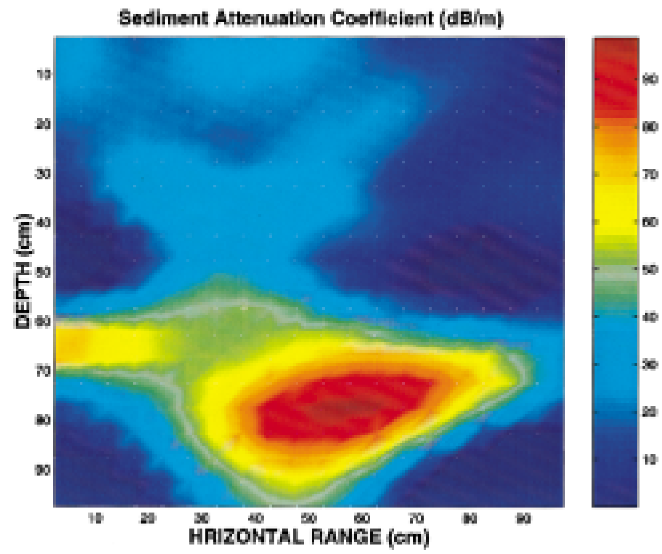

Fig. 12. Attenuation coefficient tomographic results of the muddy sediment at Hadley Harbor, MA, using (18), and the same inversion parameters as used in obtaining Fig. 11.

The inverted sound speed varies from 1340 ms^{-1} to 1650 ms^{-1}, with a mean value of 1473 ms^{-1} and a standard deviation of 55.6 ms^{-1} (3.8% of the mean sound speed) (Fig. 11). Taking into account that the values toward the bottom part (away from the horizontal probe) are less reliable than those on the top part, values of sound speed at depth between 0 to 70 cm vary between 1400 ms^{-1} to 1565 ms^{-1}, with a mean value of 1480 ms^{-1} and a standard deviation of 34.4 ms^{-1} (2.3% of the mean sound speed). However, even though the reliability of the inversion toward the bottom part is lower than that of the upper portion, the high and low sound speed patches can be checked by examining a few rays passing through this region. For example, the arrival time of channel 5 in Fig. 10 (corresponding to a depth of 75 cm) is slower than what is expected from a homogeneous medium.

To perform the attenuation inversion, the amplitude of the first peak of the waveform was used. Since the transmit signal was a chirp, the instantaneous frequency at the first peak is 96 kHz based on the theoretical transmit signal. The amplitudes were manually picked. Several patches with large and small values of attenuation are evident from the inverted image (Fig. 12), ranging from about 0 dBm^{-1} to 100 dBm^{-1}. A large patch with high values of attenuation is located in the region below 70 cm and around 40–70 cm of horizontal range. As discussed before, such a large attenuation region can be understood by examining the received waveforms. Again, if we examine the amplitudes of channels 1 to 3 in Fig. 10 carefully, we find that the amplitudes of the first peak are attenuated more than those of the other channels.

To check the inverted sound speed and attenuation results, we compare the horizontally averaged sound speed and attenuation profiles from the inverted images shown in Figs. 11 and 12 at different depths to those from the direct measurements in which the transmit and receive channels are at the same depths (Fig. 13). The two approaches yield essentially the same patterns. However, the horizontal variability of the sound speed and attenuation can only be characterized statistically by means of tomographic inversion. A pronounced low sound-speed layer located at depth about 80 cm coincides with a high attenuation layer. The values of attenuation in the upper 65 cm (20 dBm^{-1}) are in agreement with those summarized by Hamilton for muddy sediments [3]. The variation of the sound speed, however, is larger than those reported by other investigators [1], [2], [5]. A larger than expected sound-speed variability may result from any or a combination of the following possible reasons. First, the three assumptions of straight ray, single ray, and no dispersion made in our inversion scheme may be violated. Although there is no direct evidence of a layered sediment, which will result ray

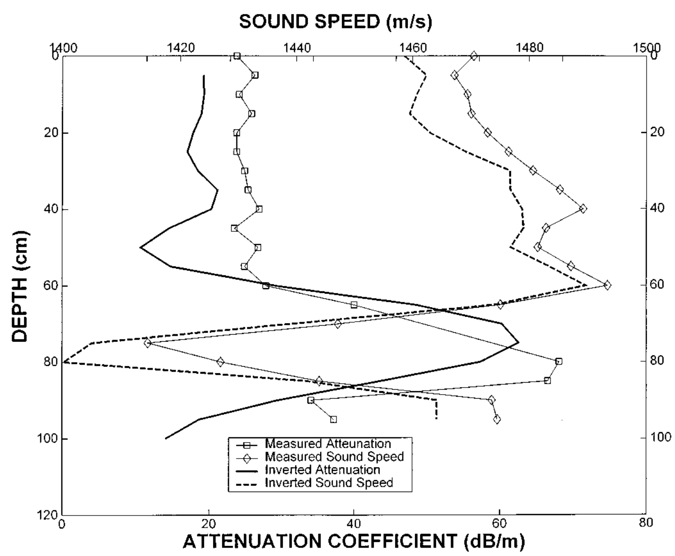

Fig. 13. Comparison between directly measured profiles and those from the inversions. The dashed line and the diamonds are, respectively, the measured and inverted sound-speed profiles, while the solid line and the squares are respectively the measured and inverted values of attenuation.

bending and multiple ray paths, the stratification cannot be ruled out. Second, scattering from broken shells could cause higher attenuation and larger sound-speed variation. Third, artifacts of the inversion may contribute to the larger sound-speed variation. However, a laboratory experiment (calibration) without the presence of the polyurethane block (not shown) yields a mean inverted sound speed of 1514 ms^{-1}, the corresponding maximum and minimum values of 1535 and 1491 ms^{-1}, respectively, and a standard deviation of 9 ms^{-1}, which is about 0.6% of the mean value. This result indicates that the inversion artifact is not significant compared to the variations shown in Fig. 11. Fourth, since the muddy sediment is rich in organic materials, the possible existence of microbubbles may result in lower and higher sound speed patches depending on the ka value of bubbles, where k is the wave number and a is the radius of the bubbles. At 100 kHz, the average spherical radius required to cause bubble resonance is 30 μm. Unfortunately, there are no data to support the presence of such bubbles. However, data collected from the soft muddy sediment at Eckernförde Bay, Germany, show that at 58 kHz, the compressional wave velocity is around 1530 ms^{-1} [5], indicating the presence of bubbles whose average spherical radius was less than 55 microns. Based on the X-ray data [42], Tang used an exponential function to describe the bubble distribution in the same area [24]. Although the minimum size of the bubble provided in Abegg *et al.* [42] is limited by the resolution of their instrument, it is possible that bubbles less than 55 microns are still significant. Since the sediment of Hadley Harbor, MA, and the sediment of Eckernförde Bay are both soft muddy sediments, it is reasonable to assume that there are microbubbles in the organic-material-rich sediment at our field experiment site.

VI. Conclusions

An acoustic tomographic imaging system has been developed to map fine-scale acoustic properties of shallow water sediments. Unlike the conventional configuration for crosshole tomography, an additional horizontal transducer array is included in our system, which greatly increases the system's spatial resolution. The system is capable of detecting and characterizing sediment inhomogeneities with spatial dimensions of a few centimeters to 10 cm in scale.

A series of numerical simulations have been presented to demonstrate the system's performance in terms of the arrival time detection error and transducer position error—two major sources of error in sediment tomography. Randomly distributed (Gaussian PDF) position errors can be corrected effectively. It is shown that for an RMS arrival time error of 500 ns and an RMS position error of 4 mm, the performance of the current tomographic system is capable of characterizing sound-speed anomalies of less than 2% within a 10-cm block.

A laboratory experiment in water with a submerged cylindrical polyurethane block (10 cm in diameter) was conducted using the tomography system. The polyurethane block is correctly located, but the results show a spatial spread from the actual dimension of the block due to diffraction. Since the sound speed in the polyurethane is more than 20% higher than that in the surrounding seawater, diffraction could be important.

Preliminary tomography results from a field experiment were presented. The sound speed and attenuation images indicate inhomogeneous characteristics of a muddy sediment. The overall sound speed varies from 1340 to 1650 ms^{-1} with a mean value of 1473 ms^{-1}, and from 1400 to 1565 ms^{-1} with a mean value of 1480 ms^{-1} in the region where the inversion is more robust. The standard deviations of the sound speed are 3.7% and 2.3%, respectively, in the corresponding regions. The reconstructed values of attenuation vary from 10 to 65 dBm^{-1} at about 95 kHz. The averaged values of attenuation profile over depth revealed that a high attenuation region, about 60 dBm^{-1} around 95 kHz, is found at about 80 cm below the horizontal probe and coincides with the low sound-speed layer, indicating possible presence of microbubbles in the muddy sediment.

Appendix

The explicit form of $\partial t/\partial x_t$, $\partial t/\partial x_r$, $\partial t/\partial z_t$, and $\partial t/\partial z_r$ for a homogeneous medium are given in [30]. To obtain an appropriate form of $\partial \mathbf{t}/\partial \mathbf{p}$ in (8), we rewrite (2) as

$$\begin{aligned} t_i &= \int_{p_t}^{p_r} s_i(\mathbf{r})|\,d\mathbf{r}| \\ &= \int_{x_t}^{x_r} s_i(x)\sqrt{1+f_i'^2}\,dx \end{aligned} \tag{A1}$$

where p_t and p_r stand for transmit and receive positions, while x_t and x_r are the x coordinates of transmit and receive positions, respectively. f_i' is the derivative, or slope, of the ith ray. The straight ray path assumption (Section II-A) results in

$$\sqrt{1+f_i'^2} = \sqrt{1+\left(\frac{z_r - z_t}{x_r - x_t}\right)^2} = \frac{r_i}{x_r - x_t} \tag{A2}$$

where $r_i = \sqrt{(z_r - z_t)^2 + (x_r - x_t)^2}$ is the length of the ith ray. Substituting (A2) into (A1) leads to

$$t_i = \frac{r_i}{x_r - x_t}\int_{x_t}^{x_r} s_i(x)\,dx. \tag{A3}$$

Differentiating (A3) with respect to x_t results in

$$\frac{\partial t_i}{\partial x_t} = \left(\frac{z_r - z_t}{x_r - x_t}\right)^2 \frac{t_{x_i}}{r_i} - \frac{r_i}{x_r - x_t}\,s_i(x) \tag{A4}$$

where $t_{x_i} = \int_{x_t}^{x_r} s_i(x)\,dx$ is the apparent time in x direction. Similarly

$$\frac{\partial t_i}{\partial x_r} = -\left(\frac{z_r - z_t}{x_r - x_t}\right)^2 \frac{t_{x_i}}{r_i} + \frac{r_i}{x_r - x_t} s_i(x) = -\frac{\partial t_i}{\partial x_t}. \tag{A5}$$

It is straightforward to obtain

$$\frac{\partial t_i}{\partial z_t} = -\left(\frac{z_r - z_t}{x_r - x_t}\right)\frac{t_{x_i}}{r_i} \tag{A6}$$

and

$$\frac{\partial t_i}{\partial z_r} = -\frac{\partial t_i}{\partial z_r} = \left(\frac{z_r - z_t}{x_r - x_t}\right)\frac{t_{x_i}}{r_i}. \tag{A7}$$

Combining the above solutions, a general form solution can be expressed as

$$\frac{\partial t_i}{\partial x_j} = \begin{cases} \left(\dfrac{z_j - z_k}{x_j - x_k}\right)^2 \dfrac{t_{x_i}}{r_i} - \dfrac{r_i}{x_j - x_k} s_i(x), \\ \quad j\text{th transducer is transmitting} \\ -\left(\dfrac{z_j - z_k}{x_j - x_k}\right)^2 \dfrac{t_{x_i}}{r_i} + \dfrac{r_i}{x_j - x_k} s_i(x), \\ \quad j\text{th transducer is receiving} \\ 0, \\ \quad j\text{th transducer is neither transmitting nor} \\ \quad \text{receiving} \end{cases} \tag{A8}$$

and

$$\frac{\partial t_i}{\partial z_j} = \begin{cases} -\left(\dfrac{z_j - z_k}{x_j - x_k}\right) \dfrac{t_{x_i}}{r_i}, \\ \quad j\text{th transducer is transmitting} \\ \left(\dfrac{z_j - z_k}{x_j - x_k}\right) \dfrac{t_{x_i}}{r_i}, \\ \quad j\text{th transducer is receiving} \\ 0, \\ \quad j\text{th transducer is neither transmitting nor} \\ \quad \text{receiving} \end{cases} \tag{A9}$$

where the subscripts j and k are the position indices of the transducer pair that constitute the ith ray. The index k can be determined once the ray number index i and the index j of the first transducer are given.

Acknowledgment

The authors are grateful to the anonymous reviewers who made many valuable suggestions.

References

[1] E. L. Hamilton, G. Shumway, H. W. Menard, and C. J. Shipex, “Acoustic and other physical properties of shallow-water sediments off San Diego,” *J. Acoust. Soc. Amer.*, vol. 28, pp. 1–15, 1956.

[2] E. L. Hamilton, “Sound velocity and related properties of marine sediments, North Pacific,” *J. Geophys. Res.*, vol. 75, pp. 4423–4446, 1970.

[3] ——, “Compressional-wave attenuation in marine sediments,” *Geophys.*, vol. 37, pp. 620–646, 1972.

[4] A. C. Kibblewhite, “Attenuation of sound in marine sediments: A review with emphasis on new low-frequency data,” *J. Acoust. Soc. Amer.*, vol. 86, pp. 716–738, 1989.

[5] M. D. Richardson and K. B. Briggs, “In situ and laboratory measurements in soft mud and hard-packed sand sediments: Implications for high-frequency acoustic propagation and scattering,” *Geomarine Lett.*, vol. 16, pp. 196–203, 1996.

[6] K. B. Briggs and M. D. Richardson, “Small-scale fluctuations in acoustic and physical properties in surficial carbonate sediments and their relationships to bioturbation,” *Geomarine Lett.*, vol. 17, pp. 306–315, 1997.

[7] K. A. Dines and R. J. Lytle, “Computerized geophysical tomography,” *Proc. IEEE*, vol. 67, pp. 1065–1073, 1979.

[8] A. J. Devaney, “Variable density acoustic tomography,” *J. Acoust. Soc. Amer.*, vol. 78, pp. 120–130, 1985.

[9] T. K. Biship, K. P. Bube, R. T. Cutler, R. T. Langan, P. L. Love, J. R. Resnick, R. T. Shuey, D. A. Spindler, and H. W. Wyld, “Tomographic determination of velocity and depth in laterally varying media,” *Geophys.*, vol. 50, pp. 903–923, 1985.

[10] S. Ivansson, “Seismic borehole tomography—Theory and computational methods,” *Proc. IEEE*, vol. 74, pp. 328–338, 1986.

[11] B. Dyer and M. H. Worthington, “Some sources of distortion in tomographic velocity images,” *Geophys. Prospecting*, vol. 36, pp. 209–222, 1988.

[12] N. D. Bregman, R. C. Bailey, and C. H. Chapman, “Crosshole seismic tomography,” *Geophys.*, vol. 54, pp. 200–215, 1989.

[13] H. Gan, R. Ludwig, and P. L. Levin, “Nonlinear diffractive inverse scattering for multiple scattering in inhomogeneous acoustic background media,” *J. Acoust. Soc. Amer.*, vol. 97, pp. 764–776, 1995.

[14] C.-H. Huang and D.-M. Wang, “A statistical analysis for an inverse acoustic problem in estimating spatially varying sound velocity,” *J. Acoust. Soc. Amer.*, vol. 101, pp. 1262–1268, 1996.

[15] S. K. Park and G. P. Van, “Inversion of pole–pole data for 3-D resistivity structure beneath arrays of electrodes,” *Geophys.*, vol. 56, pp. 951–960, 1991.

[16] M. Pilkington and J. P. Todoeschuck, “Natural smoothness constraints in cross-hole seismic tomography,” *Geophys. Prospecting*, vol. 40, pp. 227–242, 1992.

[17] R. G. Pratt and C. H. Chapman, “Traveltime tomography in anisotropic media—II: Application,” *Geophys. J. Int.*, vol. 109, pp. 20–37, 1992.

[18] Y. Sasaki, “Resolution of resistivity tomography inferred from numerical simulation,” *Geophys. Prospecting*, vol. 40, pp. 453–463, 1992.

[19] T. Yamamoto, “Velocity variabilities and other physical properties of marine sediments measured by crosswell acoustic tomography,” *J. Acoust. Soc. Amer.*, vol. 98, pp. 2235–2248, 1995.

[20] B. Rapids, T. Nye, and T. Yamamoto, “Pilot experiment for the acquisition of marine sediment properties via small scale tomography system,” *J. Acoust. Soc. Amer.*, vol. 103, pp. 212–224, 1998.

[21] D. R. Jackson, “Models for scattering from seabed,” *Proc. Inst. Acoust.*, vol. 16, pp. 161–169, 1994.

[22] K. L. Williams and D. R. Jackson, “Monostatic and bistatic bottom scattering: Recent modeling and experiments,” in *Proc. OCEAN*, vol. II, 1994, pp. 255–260.

[23] D. R. Jackson, K. L. Williams, and K. B. Briggs, “High-frequency acoustic observations of benthic spatial and temporal variability,” *Geomarine Lett.*, vol. 16, pp. 212–218, 1996.

[24] D. Tang, “Modeling high-frequency acoustic backscattering from gas voids,” *Geomarine Lett.*, vol. 16, pp. 261–265, 1996.

[25] D. Chu, K. L. Williams, D. Tang, and D. R. Jackson, “High-frequency bistatic scattering by sub-bottom gas bubbles,” *J. Acoust. Soc. Amer.*, vol. 102, pp. 806–814, 1997.

[26] S. A. Swift and R. A. Stephen, “The scattering of a low-angle pulse beam from seafloor volume heterogeneities,” *J. Acoust. Soc. Amer.*, vol. 96, pp. 991–1001, 1994.

[27] Y. Zhang and R. L. Weaver, “Scattering from a thin random fluid layer,” *J. Acoust. Soc. Amer.*, vol. 96, pp. 1899–1909, 1994.

[28] P. C. Hines, “Theoretical model of in-plane scatter from a smooth sediment seabed,” *J. Acoust. Soc. Amer.*, vol. 99, pp. 836–844, 1996.

[29] T. Yamamoto, “Acoustic scattering in the ocean from velocity and density fluctuations in the sediments,” *J. Acoust. Soc. Amer.*, vol. 99, pp. 866–879, 1996.

[30] S. D. Rajan, G. V. Frisk, J. A. Doutt, and C. J. Sellers, “Determination of compressional wave and shear wave speed profiles in sea ice by crosshole tomography—Theory and experiment,” *J. Acoust. Soc. Amer.*, vol. 93, pp. 721–738, 1993.

[31] R. G. Pratt, Z.-M. Song, P. Williamson, and M. Warner, “Two-dimensional velocity models from wide-angle seismic data by wavefield inversion,” *Geophys. J. Int.*, vol. 124, pp. 323–340, 1996.

[32] M. N. Rychagov and H. Ermert, “Reconstruction of fluid motion in acoustic diffraction tomography,” *J. Acoust. Soc. Amer.*, vol. 99, pp. 3029–3035, 1996.

[33] S. J. Norton, “Fluid flow imaging by means of wide-band diffraction tomography,” *J. Acoust. Soc. Amer.*, vol. 105, pp. 2717–2721, 1999.

[34] P. S. Carney, E. Wolf, and G. S. Agarwal, “Diffraction tomography using power extinction measurements,” *J. Opt. Soc. Amer. A*, vol. 16, pp. 2643–2648, 1999.

[35] I.-T. Lu, “Robustness of a ray travel-time inversion approach,” *J. Acoust. Soc. Amer.*, vol. 106, pp. 2442–2453, 1999.

[36] W. Menke, *Geophysical Data Analysis: Discrete Inverse Theory*. New York: Academic, 1984.

[37] C. Wunsch, *The Ocean Circulation Inverse Problem*. New York: Cambridge Univ. Press, 1996, ch. 3.

[38] H. Guan, “Multilevel algebraic reconstruction technique for x-ray computed tomography,” *Medical Phys.*, vol. 24, p. 473, 1997.

[39] A. V. Lakshminarayanan and A. Lent, “Methods of least-squares and SIRT in reconstruction,” *J. Theor. Biol.*, vol. 76, pp. 267–295, 1979.

[40] C. A. Boyles, *Acoustic Waveguides: Applications to Oceanic Science*. New York: Wiley, 1984.

[41] S. Ivansson, “A study of methods for tomographic velocity estimation in the presence of low-velocity zones,” *Geophys.*, vol. 50, pp. 969–988, 1985.

[42] F. Abegg, A. Anderson, L. Buzi, A. P. Lyons, and T. H. Orsi, “Free methane concentration and bubble characteristics in Eckernförde Bay, Germany,” in *Proc. Gassy Mud Workshop, FWG*, T. F. Wever, Ed., Keil, Germany, pp. 84–89.

Dezhang Chu received the B.S. degree in electrical engineering from China University of Geosciences, Wuhan, China, in 1982 and the Ph.D. degree in geophysices from the University of Wisconsin, Madison, in 1989.

He was a Postdoctoral Scholar at the Woods Hole Oceanographic Institution, Woods Hole, MA, from 1989 to 1990 and is currently a Research Specialist in the Woods Hole Oceanographic Institution. His research interests include acoustic scattering, wave propagation in shallow water, and seafloor characterization.

Dr. Chu is a member of the Acoustical Society of America and Sigma Xi.

Dajun Tang received the Ph.D. degree in oceanographic engineering from the MIT/WHOI Joint Program, Woods Hole, MA, in 1991.

From 1991 to 1996, he was a staff scientist at WHOI. Since 1996, he has been a Senior Oceanographer at the Applied Physics Laboratory, University of Washington. His research interests include underwater acoustics concerning shallow-water sediments.

Dr. Tang is a member of the Acoustical Society of America.

Thomas C. Austin received the M.S.E.E. degree in communications and signal processing from Northeastern University in 1987.

He has been at Woods Hole Oceanographic Institution, Woods Hole, MA, since 1990, specializing in underwater acoustic signal processing, autonomous vehicles, and seafloor observatories.

Mr. Austin is a member of the Marine Technology Society.

Alan A. Hinton (M’89) received the B.S. degree in electrical engineering technology from Purdue University, West Lafayette, IN, in 1988 and the M.S. degree in electrical engineering from the University of Massachusetts, Dartmouth, in 1996.

He worked at Woods Hole Oceanographic Institution, Woods Hole, MA, from 1989 to 1998 and is currently with Sonetech Corp. His research interests include real-time underwater acoustic signal processing, systems architecture for real-time systems, and analog and digital signal processing.

Richard I. Arthur, Jr., received the B.S. degree in mechanical engineering from Southeastern Massachusetts University in 1988.

He worked at Woods Hole Oceanographic Institution, Woods Hole, MA, from 1989 to 1998 as a mechanical engineer and is currently working as a self-employed mechanical engineer. His research interests are focused on the development of underwater instrumentation and equipment.